Journal of Materials Chemistry A

ROYAL SOCIETY OF CHEMISTRY

PAPER

View Article Online
View Journal | View Issue

Cite this: J. Mater. Chem. A, 2025, 13, 8774

Highly efficient organic solar cells enabled by ultraviolet-ozone treated molybdenum oxide hole transport layers†

Apostolos Panagiotopoulos, [a] George Kakavelakis, *[b] Kyriakos Almpanidis, [a] Leslie Askew,[a] Dimitar I. Kutsarov[a] and S. Ravi P. Silva *[a]

The application of ultraviolet ozone (UV-Ozone) treatment of thermally evaporated molybdenum oxide (MoO_x) as a hole transport layer (HTL) in non-fullerene acceptor (NFA)-organic solar cells (OSCs) has markedly improved the charge carrier transport. As a result, we report the power conversion efficiency (PCE) of PM6:Y6-based OSCs has been improved from 14.26% for pristine to 15.06% for UV-Ozone-treated devices. This PCE enhancement is attributed to increased hole mobility, more balanced mobilities ratio and higher direct current (DC) conductivity. Additionally, the formation of a more favourable interface between MoO_x and the PM6:Y6 due to the UV-Ozone exposure, resulted in longer charge carrier lifetimes. Light soaking experiments at 55 °C in a nitrogen environment demonstrated superior operational stability with pristine and UV-Ozone-treated MoO_x, retaining 58% and 65% of their initial PCE after 100 hours, respectively. This stands in contrast to devices based on PEDOT:PSS that deteriorated to 23% of their initial PCE after half the time period. This strategy is an enabler towards simultaneous improvement in performance and stability compared to the control PEDOT:PSS-based cells, presenting high efficiency but significantly lower lifetime stability. The broad applicability of UV-Ozone treatment of thermally evaporated MoO_x HTLs was further validated through the fabrication of OSCs with a PM6:L8-BO photoactive layer, achieving a peak PCE value of 16.85%. These findings indicate significant advancements in the use of transition metal oxides in NFA-based OSCs and highlight the potential for new device architectures for organic electronics.

Received 1st November 2024
Accepted 16th February 2025

DOI: 10.1039/d4ta07795d

rsc.li/materials-a

Introduction

In recent years, intense research to develop novel materials used for organic solar cells (OSCs) has resulted in power conversion efficiency (PCE) values of over 19%.[1–3] Among the emerging photovoltaic technology candidates, OSCs have shown great potential for a plethora of applications where high power-per-weight (PPW) is the key requirement.[4] Despite the successful deployment of novel electron transporting layers (ETLs)[5–10] and bulk-heterojunction (BHJ) photoactive layers,[2,11,12] the progress of hole transporting layers (HTLs) remains limited. To date, poly(3,4-ethylenedioxythiophene):poly(styrenesulfonate) (PEDOT:PSS) and carbon based derivatives[13–15] remain the commonly used materials for OSCs with a standard (p–i–n) architecture.[16,17] However, the acidic nature of PEDOT:PSS (pH = 1) and its hygroscopicity[18] are known for reducing the long-term operational stability of OSCs which commonly rely on indium tin oxide (ITO) as the transparent electrode.[19,20] Hence, a stable and efficient HTL alternative is needed for the progressing commercialization of NFA-based OSCs.[21]

Based on the potential for superior environmental stability,[22–25] transition metal oxides (TMOs) such as molybdenum oxide (MoO_x),[26] nickel oxide (NiO_x),[27] tungsten oxide (WO_3)[28] and vanadium oxide (V_2O_5)[29] have been successfully used as replacements for PEDOT:PSS in OSCs. Among the TMOs, MoO_x has received much attention due to its high optical transmittance in the visible wavelengths, suitable work function (WF), and its versatile easy processing with vacuum- or solution deposition techniques.[30,31] Even though evaporated MoO_x has already been studied as an HTL for fullerene-based OSCs,[32] it has not been deployed successfully in non-fullerene acceptor (NFA)-based systems yet. Today a handful of reports show the use of MoO_x as HTL in NFA OSCs, however there are still areas for development on the findings of these studies. More specifically, the work conducted by Brinkmann *et al.*[33] demonstrated a 16.5% PCE on binary OSCs where evaporated MoO_x was used as an HTL. In the report, the PCE was measured for devices with an active area of 0.017 cm^2, which is smaller than the standard

[a]Advanced Technology Institute, School of Computer Science and Electronic Engineering, University of Surrey, Guildford, Surrey GU2 7XH, UK. E-mail: s.silva@surrey.ac.uk; kakavelakis@hmu.gr

[b]Department of Electronic Engineering, School of Engineering, Hellenic Mediterranean University, Romanou 3, Chalepa, GR-73100, Chania, Crete, Greece

† Electronic supplementary information (ESI) available. See DOI: https://doi.org/10.1039/d4ta07795d

device areas shown in the literature (~0.1 cm^2) and accepted by most international centres for standardization (NREL, Fraunhofer *etc.*). Furthermore, studies presented by Yaozhao Li *et al.*[30] and Wisnu Hadmojo *et al.*[34] showed poor reproducibility when evaporated MoO_x was used as the HTL and with approximately 20% PCE loss compared to the reference samples based on PEDOT:PSS. The authors observed lower PCEs of the used pristine MoO_x films as HTLs compared to PEDOT:PSS in NFA-based OSCs and ascribed this to inferior charge transport and collection probabilities at the HTL/ITO interface. This inferior charge transport/collection behaviour is directly related to a poor hole mobility and an unfavourable work function of the MoO_x at the interface with the ITO transparent electrode compared to its PEDOT:PSS counterpart.

Herein, we report a facile universal post-deposition treatment on MoO_x films that leads to increased charge carrier mobilities, more balanced mobility ratio and improved energetical alignment at the TMO/active layer interface for NFA-based OSCs. In this respect, we investigate the influence of different HTLs on binary PM6:Y6 BHJ-based OSCs. Devices utilizing the UV-Ozone treated MoO_x HTL demonstrate improved PCE values peaking at 15.06% compared to the pristine MoO_x HTL with a maximum PCE of 14.26%, respectively. This identified enhancement is ascribed to an improvement in the hole mobility and mobilities ratio with a more favourable energy level alignment between the treated MoO_x HTL/ITO anode electrode upon the ultraviolet ozone (UV-Ozone treatment). Furthermore, stability studies indicate that OSCs containing PEDOT:PSS experience a rapid performance degradation to 23% of their initial PCE after 51 hours of continuous light soaking at 55 °C in nitrogen atmosphere. By replacing PEDOT:PSS with pristine and UV-Ozone-treated MoO_x we observed a significantly reduced device degradation, which provides for more stable interfaces, thus maintaining ~58% and 65% of their initial PCE after 100 hours. We also explored the applicability of UV-Ozone treated MoO_x HTL by employing a state-of-the-art binary photoactive blend PM6:L8-BO and showed that the devices achieved PCE values of 16.85%. Our study sheds light on the mechanisms underlying the performance and mainly the stability of MoO_x-based devices, which is the key parameter towards the commercialization of OSCs.

Experimental

Materials

All chemicals used in this paper were obtained commercially and used without further purification. The traditional hole conductive polymer poly(3,4-ethylenedioxythiophene):poly(styrenesulfonate) (PEDOT:PSS Al4083) was obtained from (Ossila, UK) and molybdenum(VI) oxide from (Sigma-Aldrich, UK). The polymer donor poly[(2,6-(4,8-bis(5-(2-ethylhexyl-3-fluoro)thiophen-2-yl)-benzo[1,2-*b*:4,5-*b*′]dithiophene))-*alt*-(5,5-(1′,3′-di-2-thienyl-5′,7′-bis(2-ethylhexyl)benzo[1′,2′-*c*:4′,5′*c*′]dithiophene-4,8-dione))] (PM6), the non-fullerene acceptors 2,2′-((2*Z*,2′*Z*)-((12,13-bis(2-ethylhexyl)-3,9-diundecyl-12,13-dihydro-[1,2,5]thiadiazolo[3,4-e]thieno[2″,3″:4′,5′]thieno[2′,3′:4,5]pyrrolo[3,2-*g*]thieno[2′,3′:4,5]thieno[3,2-b]indole-2,10-diyl)bis(methanylylidene))bis(5,6-difluoro-3-oxo-2,3-dihydro-1*H*-indene-2,1-diylidene))dimalononitrile (Y6) and -2,2′-((2*Z*,2′*Z*)-((12,13-bis(2-ethylhexyl)-3,9-(2-butyloctyl)-12,13-dihydro-[1,2,5]thiadiazolo[3,4-e]thieno[2″,3″:4′,5′]thieno[2′,3′:4,5]pyrrolo[3,2-*g*]thieno[2′,3′:4,5]thieno[3,2-b]indole-2,10-diyl)bis(methanylylidene))bis(5,6-difluoro-3-oxo-2,3-dihydro-1*H*-indene-2,1-diylidene))dimalononitrile (L8-BO) were purchased from (Solarmer Inc). Also, (poly((2,7-bis(2-ethylhexyl)-1,2,3,6,7,8-hexahydro-1,3,6,8-tetraoxobenzo[lmn][3,8]phenanthroline-4,9-diyl)-2,5-thiophenediyl(9,9-bis(3-(dimethylamino)propyl)-9*H*-fluorene-2,7-diyl)-2,5-thiophenediyl)) (PNDIT-F3N) was purchased from (Solarmer Inc, China). 1-Chloronaphthalene (CN) and 1,4 diiodobenzene (DIB) were obtained from (Sigma-Aldrich, UK) and (Merck, UK) respectively. Chloroform (CF) and methanol (MeOH) were purchased from (Thermofisher, UK) and (Sigma-Aldrich, UK) respectively.

Substrate cleaning and preparation

Patterned indium tin oxide (ITO)-coated glass substrates purchased from Hunan Xiangcheng Ltd (China) (20 mm × 20 mm with a thickness of 1.1 mm and a sheet resistance < 15 Ω sq^{-1}) were first cleaned by sonicating in a 2% v/v Hellmanex in water solution for 20 min. The substrates were then rinsed with deionized water and sonicated in water for a further 15 min. Thereafter, they were sequentially cleaned in acetone, 2-propanol, and methanol in an ultrasonic bath at ≈40 °C for 15 min each and blow-dried with nitrogen. Before coating the substrates were subjected to an UV-Ozone process (Jetlight Company In. MODEL 24) for 15 min before fabrication. On top of the precleaned substrates a ~25 nm-thick PEDOT:PSS thin film was deposited onto the indium tin oxide surface by spin-coating and baked at 150 °C for 15 min. For the molybdenum-based devices the treated ITO substrates were loaded to an evaporator (Moorfield) placed outside the glove box and the precursor of molybdenum(VI) oxide was thermally evaporated at low rates to obtain a ~5 nm-thick MoO_x thin film. Then the samples were transferred again for UV-Ozone (Jetlight Company In. MODEL 24) for 2.5 min exposure before fabrication. The solutions of PM6 : Y6 (1 : 1.2 w/w, 16.5 mg ml^{-1} in total), in chloroform with 1-chloronaphthalene (0.5% v/v) and PM6 : L8-BO (1 : 1.2 w/w, 16.5 mg ml^{-1} in total) in chloroform with 1,4-diiodobenzene as a solid additive (the content of 1,4-diiodobenzene is 50% of the total mass of donor and acceptor) were advance and then spin-coated on top of the PEDOT:PSS layer. The prepared films were treated with thermal annealing at 100 °C for 10 min for the PM6:Y6 cells and 85 °C for 5 min for the PM6:L8BO respectively. After cooling to room temperature, a ~5 nm-thick PNDIT-F3N (0.5 mg ml^{-1} in methanol with 0.5% acetic acid, v/v) was spin-coated on the top of the active layer. Then, the samples were transferred into the evaporating chamber Angstrom EvoVac system inside the glove box and a 100 nm-thick silver (Ag) layer was thermally evaporated on the PNDIT-F3N layer.

Current (*I*)–voltage (*V*) characteristics

I–V characteristics of the fabricated solar cells were evaluated using an Enlitech SS-F5-3A (Class 3A) solar simulator with a Keysight 2901A source measure unit acting as the electrical load. The calibration of the simulator was carried out using a KG-5 filtered Si diode. A mask with 0.09 cm^2 aperture area was

used to define the active area of the device. The physical area of the device (the overlap between the top and bottom electrodes) was approximately 0.25 cm^2. All devices were measured without any encapsulation under ambient conditions at a temperature of ~25 °C and relative humidity of 30–35%, with a light intensity of 100 mW cm^{-2} (AM1.5G), calibrated using a reference cell purchased from Fraunhofer ISE CalLab (ISE001/013-2018).

External quantum efficiency (EQE), internal quantum efficiency (IQE)

EQE measurements of the fabricated devices were carried out using a Bentham PVE300 system. All measurements were carried out under ambient conditions. The monochromatic light intensity was calibrated by a traceable silicon reference detector (300–1100 nm) from the national metrology institute (NMI). All devices were measured without any encapsulation under ambient conditions at a temperature of ~25 °C and a relative humidity of 30–35%. For each device, a 0.16 cm^2 mask was used during the measurement to ensure the probing beam (size is 2.2 mm × 2.2 mm) fully inside the electrode area. The IQE was calculated by the equation: IQE = EQE/(1 − R). The reflectance spectra were performed on a Varian Cary 5000 UV-vis-NIR spectrophotometer. In Reflectance mode the measurements were obtained by fitting the spectral and diffuse reflectance accessory (integrated sphere).

Light soaking testing

For light soaking stability test, samples were illuminated in nitrogen chamber at a temperature of ~55 °C, light intensity of equivalent of one-sun (100 mW cm^{-2}) using LED 6500 K light source. All devices were measured without any encapsulation under ambient conditions during the various time points during the test.

Contact angle

The contact angles were measured using a contact angle analyzer (Drop shape analyzer-DSA25, KRÜSS GmbH). DI water dropped on the surface of the samples and measured in the air under room temperature.

Ultraviolet-visible (UV-vis) absorption, transmittance spectra

The transmittance and absorption spectra were performed on a Varian Cary 5000 UV-vis-NIR spectrophotometer.

Atomic force microscopy (AFM)

AFM images were obtained using Bruker Dimension Edge in tapping mode with scanning area size of 50 μm x 50 μm for each sample.

Photoluminescence (PL)

For the PL spectra a Horiba Xplora Plus used to obtain the spectra with the use of a 532 nm laser at 50×/0.5 mag/numerical aperture and 1200 grating.

Results and discussion

Transmittance and absorbance properties

The thickness of the MoO_x layer is vital for fabricating highly efficient OSCs as it affects the optical transmittance and electrical properties (charge transport and extraction) of the layer.[32] Therefore, we optimized the MoO_x layer thickness by fabricating OSCs with MoO_x thicknesses from 2.5 nm, 5 nm, 7.5 nm, and 10 nm (for thicknesses > 5 nm we observed a loss of performance), (see ESI S5†). Transmittance spectra, as shown in Fig. 1(a) indicates that the ITO/MoO_x (5 nm thick) anode exhibited higher transparency compared to PEDOT:PSS (~30 nm) in the wavelength ranges 460 to 620 nm and 740 to 1000 nm. At shorter wavelengths below 440 nm, the PEDOT:PSS deposited on top of ITO is more transmissive than bare ITO due to refractive index matching.[35] Such an anti-reflection effect is attributed to the optical interference between the organic layer PEDOT:PSS and inorganic ITO layer due to large refractive index (n) difference.[36] However, as shown (ESI S1 and S2†) by the absorption spectra of the photoactive blends PM6:Y6 and PM6:L8-BO, this increased transmission does not contribute much towards the photocurrent generation, due to the limited number of solar photons absorbed by the blends at this wavelengths of the solar spectrum.

Despite their high transmittance in the visible wavelengths, MoO_x films show poor electrical characteristics, and an unfavourable work function value compared to organic semiconductors such as PEDOT:PSS.[37] In the present study we use UV-Ozone treatment to modify and improve the electrical and interfacial properties of MoO_x films. UV-Ozone treatment is widely used in the field of electronics and optoelectronics for cleaning and modifying purposes with the use of photosensitized oxidation process.[38] It is known that molecular oxygen excited by ultraviolet light can dissociate to form atomic oxygen; each atomic oxygen combines with a molecular oxygen to form an ozone molecule. Ozone (O_3) has one more oxygen atom than the atmospheric oxygen. As a result, this third loosely-bonded oxygen atom can effectively destroy contaminants, which is key to its strong oxidizing properties.[32,39–41] Also, applying UV-Ozone treatment to ITO is expected to improve OSCs performance by increasing the hole-extraction efficiency.[41]

Kelvin probe measurements

Firstly, kelvin probe (KP) measurements were performed to determine the WF before and after the deposition of HTL layers on top of the ITO. For each sample, three measurements across the surface of the sample were carried out in order to evaluate the uniformity of the deposited HTL layers and the corresponding WF reproducibility.[42] For the KP the contact potential difference (CPD) between a sample and a tip was calibrated. The WF of the sample can then be determined by the WF of the tip calibrated against a known surface. In our case, freshly cleaved Highly Order Pyrolytic Graphite (HOPG) was used to calibrate the tip WF. The HOPG WF is 4.48 eV as confirmed in the literature through ultraviolet photoelectron spectroscopy (UPS).[43] To convert the contact potential difference measurement to work

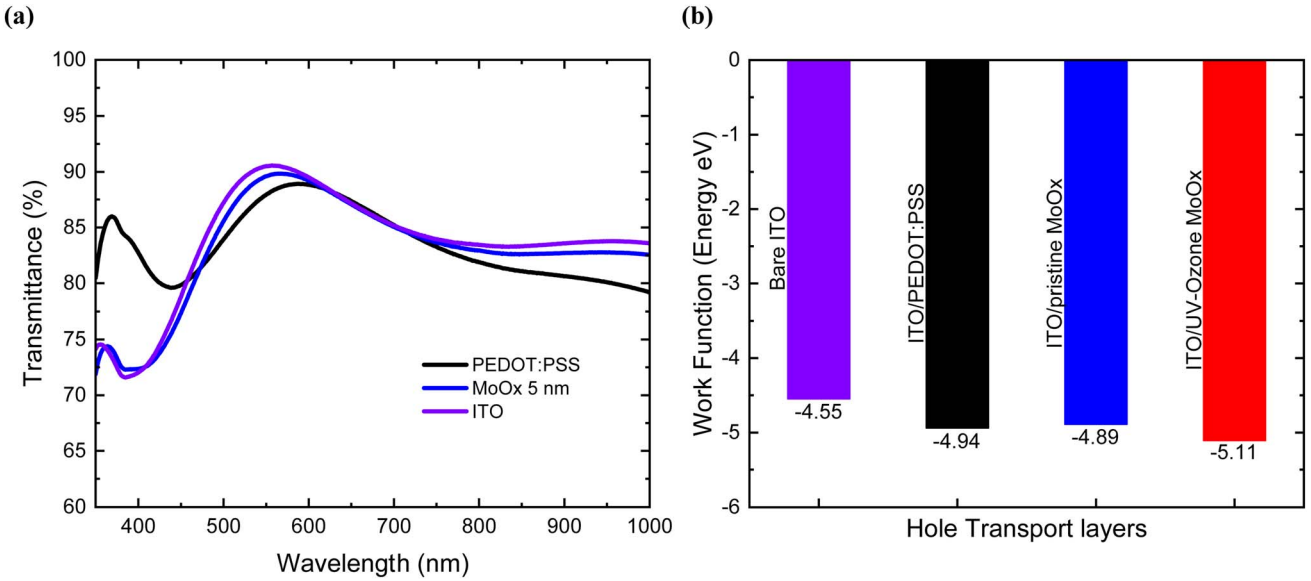

Fig. 1 (a) Transmittance spectra of ITO, ITO/pristine MoO_x, ITO/PEDOT:PSS, (b) KP measurements values of the different HTLs on top of ITO.

function, the following equations are used to determine the tip and sample WF values:

$$\text{WF of tip} = \text{WF of test sample} - \text{CPD (measured)}$$

$$\text{WF of sample} = \text{WF of Tip} + \text{CPD}$$

Generally, for thick layers of MoO_x the predominant oxidation state is Mo^{6+} while for thinner MoO_x layers it has been observed that closer to the interface, additional oxidation states of Mo^{5+}, Mo^{4+}, and Mo^{2+} arise, possibly due to an increased number of oxygen vacancies.[33] As expected from literature during the process of UV-Ozone treatment process of MoO_x films, the vacant sites are filled with oxygen atoms (O_3 can oxidize large quantities of Mo^{5+} to Mo^{6+} oxidation state) and as a result the MoO_x films become nearly stoichiometric.[32,44] Furthermore, an increased proportion of Mo^{6+} in MoO_x films leads to a higher work function. Our measurements also

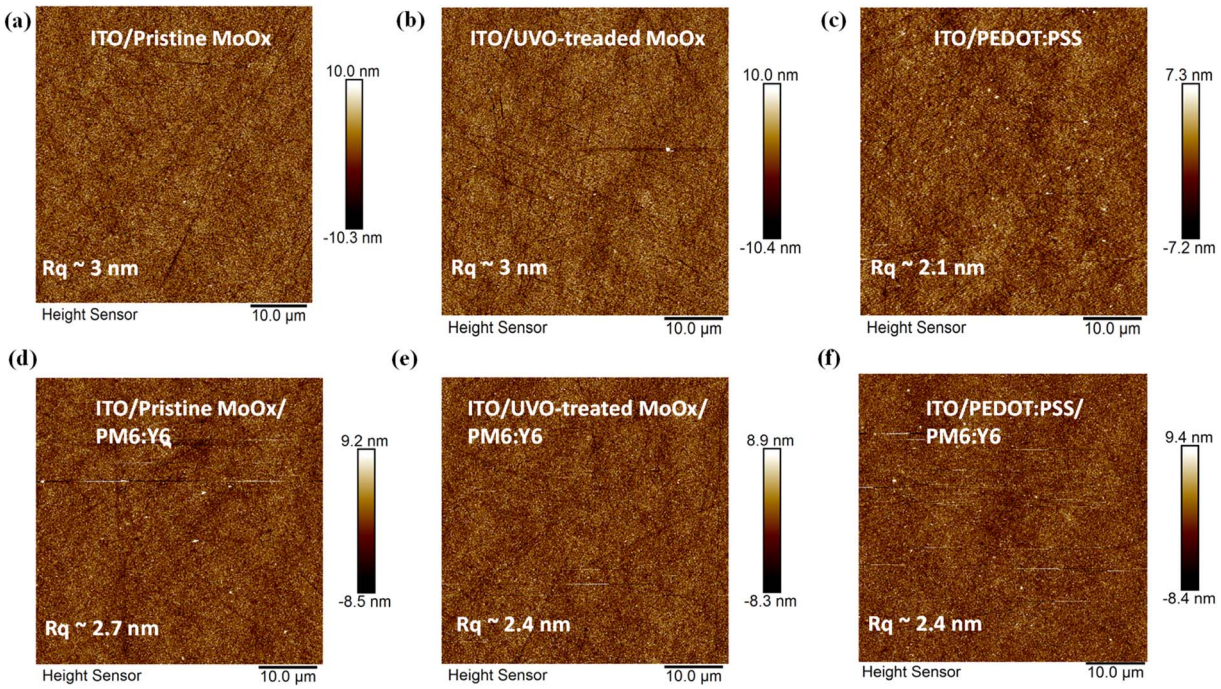

Fig. 2 AFM images and RMS roughness of the different HTLs films on top of ITO (a) ITO/pristine MoO_x, (b) ITO/UV-Ozone-treated MoO_x, (c) ITO/PEDOT:PSS films. PM6:Y6 BHJ system on top of (d) ITO/pristine MoO_x, (e) ITO/UV-Ozone-treated MoO_x and (f) ITO/PEDOT:PSS.

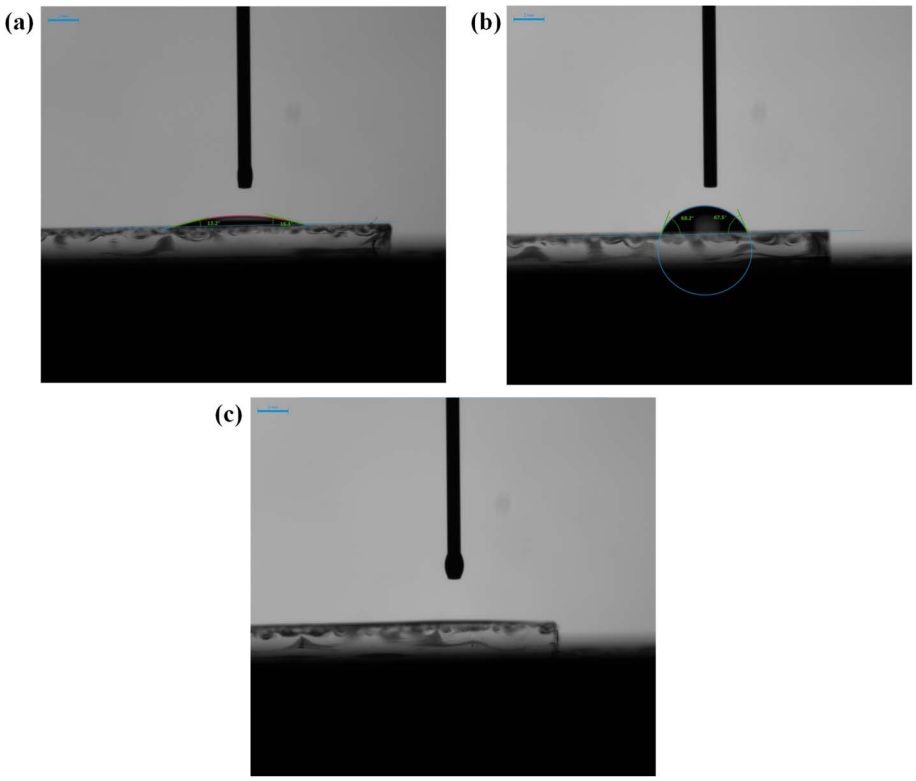

Fig. 3 Contact angle images of (a) ITO/PEDOT:PSS, (b) ITO/pristine MoO_x and (c) ITO, ITO/UV-Ozone-treated MoO_x films.

showed a clear increase of 0.2 eV (in absolute values) of MoO_x WF from $(-4.89 \pm 0.02$ eV)[45,46] to $(-5.11 \pm 0.03$ eV) after the UV-Ozone treatment was confirmed directly using KP measurements as shown in Fig. 1(b). Additionally, previous studies of ITO MTO/Ag/MTO multilayer transparent electrode demonstrate that in the case of the pristine MoO_x films, Mo^{6+} cations adjacent to the oxygen vacancies (loss of oxygen atom from their respective position in the crystal lattice) within the MoO_x lattice, undergo reduction to Mo^{5+} oxidation state by gaining a free electron in the conduction band. On the contrary, following the application of UV-Ozone treatment on MoO_x films the reduction of oxygen vacancies during this process limits the generation of excess electrons, leading to an increase in the WF.[44] This downshift of the WF of treated MoO_x samples is highly desired as it will lead to a more preferable energetic alignment with PM6 organic semiconductor used as a polymer donor in the OSC devices. This energy level alignment is expected to facilitate better hole extraction and collection in the devices using treated MoO_x HTLs. Also, the obtained WF values for the bare ITO were measured at $(-4.55 \pm 0.05$ eV) and in the case of ITO/PEDOT:PSS at $(-4.94 \pm 0.02$ eV), respectively.

Atomic force microscopy

Tapping-mode Atomic Force Microscopy (AFM) was used to determine the surface topography of the anode films. The ITO/pristine MoO_x and ITO/UV-Ozone-treated MoO_x, as shown in Fig. 2, demonstrate root-mean-square surface roughness (R_q) values of $(3.0 \pm 0.02$ nm). In comparison, the ITO/PEDOT:PSS sample exhibited an R_q value of $(2.1 \pm 0.01$ nm). We also investigated the morphology of PM6:Y6 films deposited on top of the different HTLs. There is a known relation between the charge transport properties within the bulk-heterojunction and the nanoscale phase separation of the donor and acceptor materials.[47] The AFM height images reveal R_q values of $(2.7 \pm 0.01$ nm), $(2.4 \pm 0.02$ nm), and $(2.4 \pm 0.01$ nm) for the PM6:Y6 layers deposited on top of pristine MoO_x, UV-Ozone-MoO_x, and PEDOT:PSS, respectively. Thus, we can postulate the UV-Ozone-treatment of MoO_x does not have an impact on the deposition and the surface morphology of the photoactive layer, which is essential for the efficient operation of the device. On the other hand, we observe a slight increase in R_q for the untreated MoO_x-based samples, which might a reason for the inferior HTL/Active layer interface of OSC reported in the prior art.

Contact angle measurements

The effect of the UV-Ozone treatment on the surface energy of MoO_x layers was further analysed with the contact angle measurement technique. As shown in Fig. 3, DI water was drop casted on top of the films to measure the contact angle formed between the droplet and the HTL layer (see Table 1). The ITO/

Table 1 Contact angles of H_2O on ITO/PEDOT:PSS, ITO/pristine MoO_x, and ITO/UV-Ozone-treated MoO_x

Sample	H_2O contact angle
ITO/PEDOT:PSS	$(13 \pm 1°)$–$(16 \pm 2°)$
ITO/pristine MoO_x	$(67 \pm 2°)$–$(68 \pm 2°)$
ITO/UV-Ozone-treated MoO_x	—

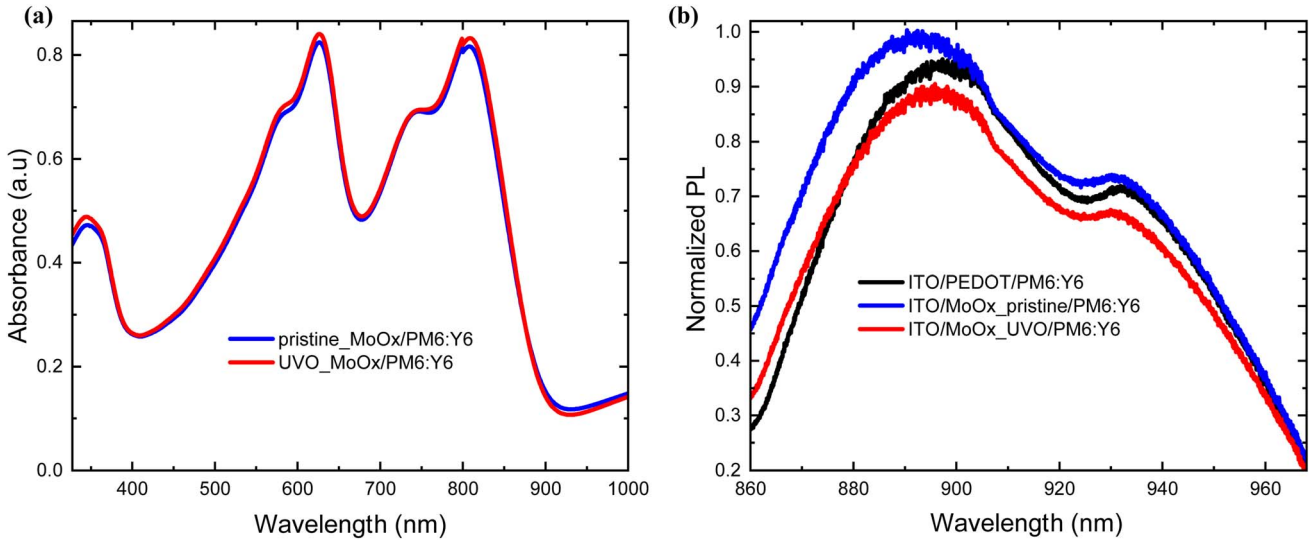

Fig. 4 (a) Absorbance of PM6:Y6 on both pristine and UV-Ozone-treated MoO_x films, (b) normalized PL intensity of PM6:Y6 BHJ system with the various HTLs.

PEDOT:PSS films exhibited contact angle values between (13 ± 1)° to (16 ± 2°) whereas the pristine MoO_x showed an increased contact angle of (67 ± 2°) to (68 ± 2°). In the case of UV-Ozone-treated MoO_x films, a significant reduction in the contact angles of the DI water droplet was observed, resulting to an angle below the detectivity limit of the camera.[44] Since UV-Ozone treatment synergistically introduces oxygen (increases the oxygen content), effectively removing hydrocarbon contaminants from the MoO_x surface and change a of stoichiometry eventually increases its surface energy. Thus, after applying UV-Ozone treatment, the MoO_x surface is more hydrophilic for the BHJ deposition, which facilitates an improved material wetting and surface contact with the PM6:Y6 layer, as confirmed by the AFM measurements and the lower R_q values.

Photoluminescence (PL)

Besides the surface and work function properties, we also performed electrical and optical characterization to explore the potential of UVO-treated MoO_x over pristine MoO_x and PEDOT:PSS. The experimental conditions used to optimize the MoO_x as HTL onto ITO (*e.g.*, thickness and UV-Ozone exposure time of evaporated MoO_x films) are shown in (ESI S3 and S4†). The optimum conditions for the thickness and UV-Ozone post-treatment exposure time of the evaporated MoO_x, revealed it to be 5 nm and 2.5 minutes respectively.

Based on the absorbance spectra of the active layer cast on top of the pristine and UV-Ozone-treated MoO_x HTL, there is negligible difference with a slightly enhanced absorbance strength at wavelengths 350, 610, and 800 nm as shown in Fig. 4(a). To get an insight into the charge extraction properties

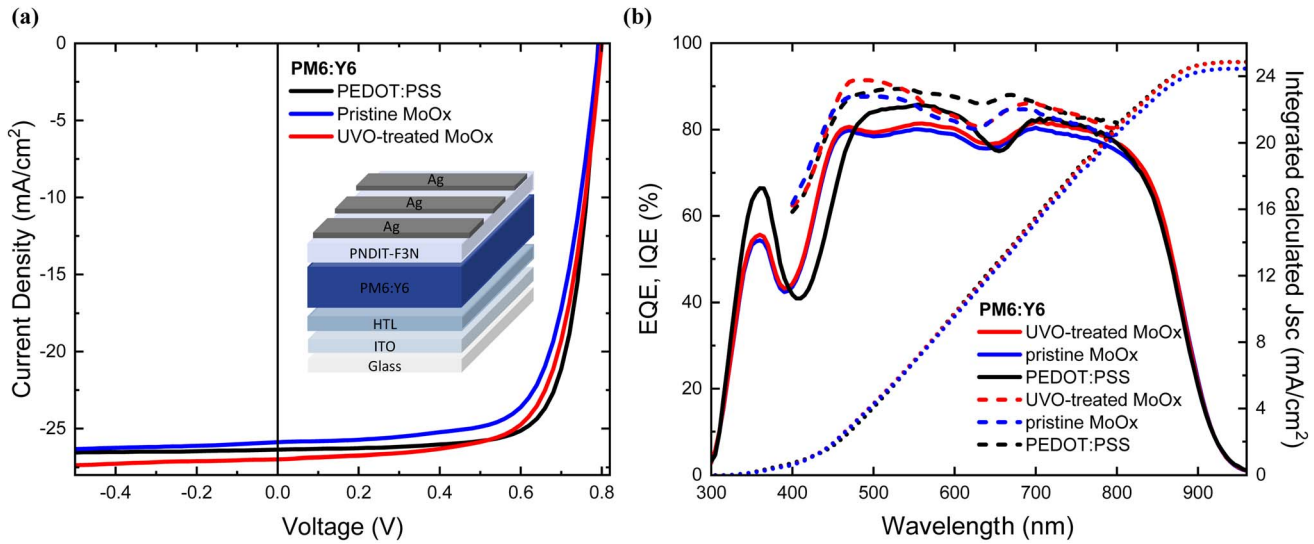

Fig. 5 (a) *J*–*V* curves of champion cells PM6:Y6 solar cells incorporating different HTLs, (b) EQE and IQE spectra of PM6:L8BO solar cells incorporating different HTLs.

Table 2 Photovoltaic parameters of PM6:Y6-based OSCs with the incorporation of the different HTLs, mean values and champion device performance in brackets

HTL	V_{oc} mean ($V_{oc\ hero}$) (V)	J_{sc} mean ($J_{sc\ hero}$) (mA cm^{-2})	J_{sc} EQE (mA cm^{-2})	FF mean (FF_{hero})	PCE mean (PCE_{hero}) (%)
PEDOT:PSS	0.80 (0.80)	26.20 (26.37)	24.88	71.75 (74.87)	15.10 (15.60)
Pristine-MoO_x	0.80 (0.80)	26.05 (25.88)	24.46	67.13 (69.40)	14.10 (14.26)
UVO-treated MoO_x	0.79 (0.80)	26.90 (26.97)	24.90	69.12 (69.77)	14.73 (15.06)

of the photogenerated carriers from the BHJ active layer to the different HTLs, the steady-state photoluminescence (PL) spectra were measured as illustrated in Fig. 4(b). It is evident that an increased PL quenching at peak (~15%) for the UV-Ozone-treated MoO_x relative to the pristine MoO_x, proving that the treatment has enhanced the rate of carrier extraction at the HTL/PM6:Y6 interface.[48]

Photovoltaic performance

To understand the effect of the UV-Ozone treatment on the device performance, p–i–n (normal) OSCs were fabricated incorporating the different HTLs. The representative *J–V* curves obtained from the champion cells are shown in Fig. 5(a), with a summary of the device photovoltaic parameters provided in

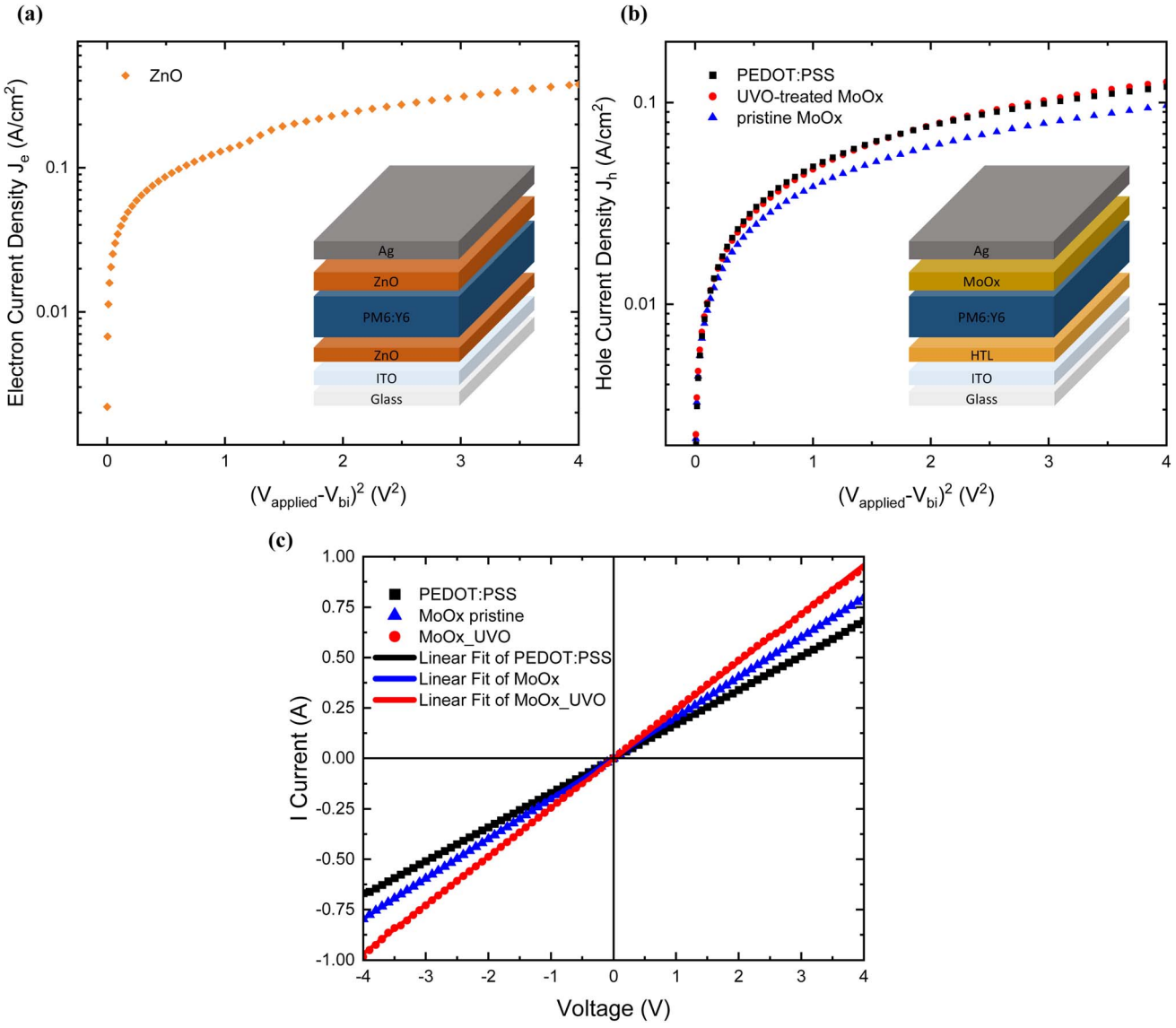

Fig. 6 (a) Dark current through electron-only device-based ITO/ZnO/PM6:Y6/ZnO/Ag, (b) dark current through hole-only device based on PEDOT:PSS, pristine MoO_x and UV-Ozone MoO_x and (c) *I–V* characteristics of conductivity measurements for ITO/PEDOT:PSS/Ag.

Table 2. The statistical analysis of experimental data obtained from 8 individual cells is furthermore shown in ESI S6.†

As summarised in Table 2, the PEDOT:PSS-based OSCs demonstrated a maximum PCE of 15.60% on 0.09 cm^2 active area, which is comparable to the published results for PM6:Y6 based OSCs (15.70%) with a standard device architecture.[49] Cells with pristine MoO_x exhibit a maximum PCE of 14.26% with J_{sc} of 25.88 mA cm^{-2}, an open circuit voltage (V_{oc}) of 0.8 V, and a fill factor (FF) of 69.40. Remarkably, 2.5 minutes of UV-Ozone exposure of MoO_x improve the device performance with a maximum PCE of 15.06% was measured. This is due to an increased J_{sc} of 26.97 mA cm^{-2} and an FF of 69.77, compared to the reference device with a pristine MoO_x.

Thus, we observe a significant improvement in PCE of 5.5% compared to untreated MoO_x OSCs and a PCE comparable to the PEDOT:PSS-based devices. The J_{sc} improvement is also confirmed by the calculated EQE photocurrent densities, which follow a similar trend to those obtained from the *J–V* curves as shown in Table 2. To further validate the improvement achieved through UV-Ozone treatment, the internal quantum efficiency (IQE) of each OSC was assessed. The MoO_x cells subjected to treatment exhibited higher internal photon-to-electron conversion efficiency in the wavelength range of 450–620 nm and 680–800 nm compared to the untreated MoO_x-based cells Fig. 5(b), ultimately leading to higher FF and increased J_{sc}.[11] This improvement can be further supported by the reduced charge interface recombination and enhanced charge extraction, as evidenced by the transient analysis later in this case study. The UV-Ozone treated MoO_x-based cells exhibited a maximum values of 92% at 480 nm in comparison to the pristine cells which showed a maximum values of 88% at 450 nm respectively. The higher average IQE spectrum for the treated cells indicates that a larger number of absorbed photons is actually converted into electrons, which are subsequently collected at the corresponding electrodes.

DC conductivity of the different HTLs

To further understand the origin of the PCE enhancement for the UV-Ozone-treated MoO_x samples compared to the pristine MoO_x, glass-ITO/HTL/Ag-based devices were fabricated in order to get an insight on the electrical conductivity of the different HTL. Fig. 6(c) depicts the *I–V* characteristics for devices with PEDOT:PSS, pristine MoO_x and UV-Ozone-treated MoO_x used as HTLs. The direct current (DC) conductivity (σ_0) can be determined from the slope of the *I–V* plot using the following equation:

$$\sigma_0 = \left(\frac{I}{V}\right)\left(\frac{d}{A}\right)$$

where *A* is the physical active area of the samples (0.25 cm^2), and *d* is the thickness of different HTL layers. The thickness of pristine MoO_x and UV-Ozone-treated films was 5 nm, and in the case of PEDOT:PSS 30 nm. The value for the conductivity of PEDOT:PSS was calculated to $2.20 \pm 0.11 \times 10^{-5}$ S cm^{-1}, whereas the DC conductivity of pristine MoO_x and UVO-treated showed values of $0.40 \pm 0.17 \times 10^{-7}$ S cm^{-1} and $0.48 \pm 0.20 \times 10^{-7}$ S cm^{-1} respectively and in line with the literature reports (DC conductivity region $10^{-13} \leq \sigma_0 \leq 10^{-4}$).[50] This implies that the UV-Ozone treatment leads to an enhancement of σ_0 by 20%. The significance of this increase lies in addressing the primary concern associated with MoO_x-based HTL in OSCs, which is their relatively poor electrical performance stemming from inherently low conductivity. This improvement further corroborates the increased J_{sc} observed alongside the reduced PL intensity in these devices. Additionally, the lower conductivity of the MoO_x-based samples compared to PEDOT:PSS, justifies the need for significantly thinner (5 nm) MoO_x films compared to (30 nm) PEDOT:PSS for optimal device operation (the lower the conductivity the thinner the HTL needs to be to prevent change accumulation).[51,52]

Charge carrier mobility measurements

The evaluation of hole and electron transport properties of the OSCs was conducted through the fabrication of structures tailored for hole-only devices (HOD) and electron-only devices (EOD), as shown in Table 3. The following architectures fabricated for this purpose including ITO/HTL/PM6:Y6/MoO_x/Ag and ITO/ZnO/PM6:Y6/ZnO/Ag respectively. The hole mobility values for each HTL (PEDOT:PSS, pristine or UV-Ozone MoO_x) and the electron mobility for (ZnO) were calculated based on the Mott–Gurney equation respectively:[53]

$$J_{SCLC} = \frac{9}{8}\varepsilon_0\varepsilon_r\mu_h\frac{\left(V_{applied} - V_{bi}\right)^2}{d^3},$$

in which ε_r is the relative dielectric constant, ε_0 is the permittivity of free space, μ_h or μ_e is the hole and electron mobility respectively, $V_{applied}$ is the applied voltage, V_{bi} is the built-in potential, and *d* is the thickness of the active layer.

The hole mobility for the reference OSCs based on PEDOT:PSS was 1.98 ± 0.01 cm^2 V^{-1} s^{-1}, in line with literature reports.[54] On the other hand, the hole mobility for the pristine MoO_x HTL films was calculated at $1.85 \pm 0.01 \times 10^{-4}$ cm^2 V^{-1} s^{-1}, while the UV-Ozone-treated MoO_x HTL films demonstrated a 10% enhancement compared to the pristine MoO_x HTL films with value of 2.01 ± 0.01 cm^2 V^{-1} s^{-1}. The higher device hole charge carrier mobility in UVO-treated MoO_x films most likely originates from the observed improved conductivity and

Table 3 Electron and hole mobility values of the EOD and HOD devices

Sample	μ_h (cm^2 V^{-1} s^{-1})	μ_e (cm^2 V^{-1} s^{-1})	Ratio (μ_h/μ_e)
PEDOT:PSS	$(1.98 \pm 0.01) \times 10^{-4}$	$(1.95 \pm 0.01) \times 10^{-4}$	1.01
UV-ozone-treated MoO_x	$(2.01 \pm 0.01) \times 10^{-4}$	$(1.95 \pm 0.02) \times 10^{-4}$	1.03
Pristine MoO_x	$(1.85 \pm 0.01) \times 10^{-4}$	$(1.95 \pm 0.01) \times 10^{-4}$	0.95

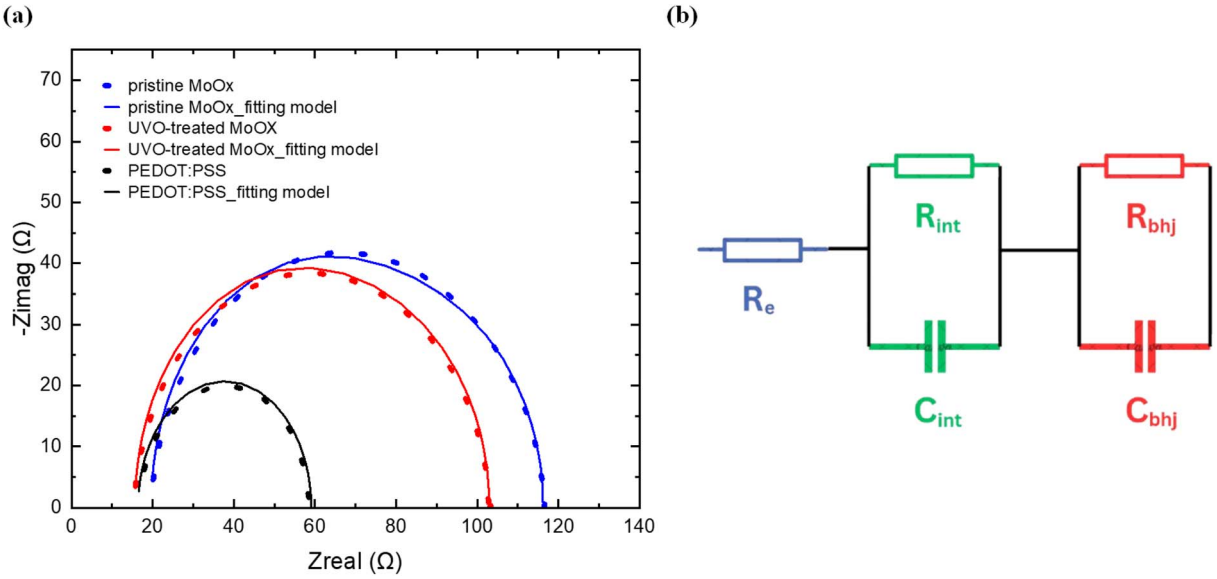

Fig. 7 (a) Nyquist plots of the EIS data with the equivalent fitting models for various HTL-based OSCs. (b) The equivalent circuit model for EIS data fitting the different OSCs.

enhanced wettability for the PM6:Y6 layer on top of the UV-Ozone treated MoO_x as shown by the DC conductivity and contact angle measurements, respectively. This results also is in excellent agreement with the observed enhanced rate of carrier extraction at the HTL/PM6:Y6 interface shown by the PL analysis. In addition, the calculated μ_e values for the PM6:Y6 blend were reproducible $1.95 \pm 0.02 \times 10^{-4}$ cm^2 V^{-1} s^{-1} and consistent with the literature.[54] The balanced ratio between the charge carrier mobility (μ_h/μ_e close to 1) is of paramount importance for obtaining high J_{sc} and FF.[55] The ratio plays a vital role in mitigating charge accumulation within the device.[56] An imbalance in the mobility of charge carriers results in the formation of a positive space charge at the photoanode, which consequently causes the trapping of electrons near the back electrode in the BHJ OSCs.[53,57] Thus, the cell utilizing PEDOT:PSS displayed a μ_h/μ_e ratio of 1.01, signifying the highest level of mobility balance among the three device types. On the other hand, the UV-Ozone MoO_x cell demonstrated a considerably more balanced mobility ratio of 1.03 than the device with the untreated MoO_x with a ratio 0.95 which reduces the charge accumulation effect leading to improved J_{sc} and FF values.[58]

Charge carrier lifetime

To get an additional insight on the operation of our OSCs, we performed electrochemical impedance spectroscopy (EIS) measurements which provides important insights related to the charge extraction and lifetime.[59] EIS measurements were performed to examine the transient behaviour in the various OSCs fabricated in this work. Thus, the measurements were obtained, in dark conditions from 1 Hz to 1 MHz, with DC bias equal to the V_{oc} for each device.[60] The Nyquist plots and the fitting model shown in Fig. 7(a) were fitted by using the equivalent circuit model[61,62] shown in Fig. 7(b) while the relevant data for each HTL type are summarized in Table 4.

The R_e corresponds to electrode resistance (ITO and Ag); R_{int} and C_{int} in parallel correspond to the interface layer's resistance and capacitance, and R_{bhj} and C_{bhj} in parallel correspond to the resistance and capacitance of the bulk heterojunction, respectively. The performance of the OSCs can be correlated by analyzing the R_{int} of the interface layer in conjunction with the average carrier transition lifetime (τ).[62–64] The reduced R_{int} values for the UV-Ozone-treated MoO_x cells (29.79 Ω) further confirms its enhanced interface conductivity compared to the pristine MoO_x (33.87 Ω) which supports our findings regarding the higher FF values obtained in UV-Ozone-treated MoO_x cells.[65] Moreover the τ values for each HTL type were calculated based on the following equation:

$$\tau = R_{bhj} \cdot C_{bhj}$$

The τ values for the pristine, the treated MoO_x and the PEDOT:PSS were calculated as 2.63 μs, 2.87 μs and 3.30 μs respectively. The longer τ values for the treated MoO_x-based

Table 4 Summary of the fitting parameter used to describe the Nyquist plots

Sample	R_e (Ω)	R_{int} (Ω)	C_{int} (nF)	R_{bhj} (Ω)	C_{bhj} (nF)	τ (μs)
Pristine MoO_x	19.60	33.87	285	62.79	41.98	2.63
UV-ozone-treated MoO_x	15.42	29.79	270.7	57.56	50.83	2.87
PEDOT:PSS	16.40	20.86	95.30	21.8	149.3	3.30

OSCs compared to the pristine is associated with a reduced the trap-assisted recombination,[66] which is also confirmed by the PL measurements (15% PL quenching at peak for the UV-Ozone-treated samples compared to the pristine). Overall the EIS findings underscore the benefits of UV-Ozone treatment on MoO_x, which contributes to reduced charge recombination and improved charge extraction to the electrodes compared with the pristine MoO_x, ultimately enhancing the FF and J_{sc}.[67]

Exciton generation

To gain a better insight into the exciton generation and dissociation processes, the dependence of the photocurrent densities (J_{ph}) of the cells with the different HTLs was plotted *versus* the effective voltage (V_{eff}), from which the maximum exciton generation rate (G_{max}) and charge collection probabilities $P(E, T)$ were calculated. J_{ph} is determined as $J_{ph} = J_L - J_D$, where J_L and J_D are the current densities under illumination and dark conditions, respectively. V_{eff} is determined as $V_{eff} = V_0 - V_a$, where V_0 is the voltage at the point of $J_{ph} = 0$, and V_a is the applied bias voltage. If we assume that the saturated current density (J_{sat}) is defined by the total quantity of the absorbed photons and all the photogenerated excitons are dissociated to free charge carriers at higher voltage (>1 V), then G_{max} can be extracted by the formula $J_{sat} = qG_{max}L$.[53,68] The values of G_{max}, as calculated from Fig. 8(a) were 1.66×10^{28} s^{-1} m^{-3} (267 A m^{-2}) for the PEDOT:PSS-based cells, 1.64×10^{28} s^{-1} m^{-3} (263 A m^{-2}) for the UV-Ozone-treated MoO_x-based cells and 1.63×10^{28} s^{-1} m^{-3} (261 A m^{-2}) for the pristine MoO_x-based cells. Fundamentally, the G_{max} is correlated to the maximum absorption of incident photons.[69,70] The almost unchanged values of G_{max} suggest that the overall exciton generation upon samples based on PEDOT:PSS and MoO_x is approximately the same. This can further be supported by the transmission spectra of the different HTLs and the nearly identical absorbance spectra strength of PM6:Y6 on top of both pristine and UV-Ozone-treated MoO_x films, as demonstrated in Fig. 1(a) and 4(a).

Charge collection probabilities

On the other hand, the charge collection probability, $P(E, T)$, can be calculated from the ratio of J_{ph}/J_{sat}.[71] Under short circuit conditions for the reference PEDOT:PSS cells, the $P(E, T)$ was estimated at (96 ± 1%), while the samples based on pristine and UV-Ozone-treated MoO_x devices exhibited values of (95 ± 1%) and (93 ± 2%), respectively Fig. 8(b). The increased $P(E, T)$ values of samples PEDOT:PSS and UV-Ozone-treated MoO_x suggested more efficient charge collection compared to the pristine MoO_x cells. These results can be further correlated by the higher values of FF as presented by the statistical analysis distribution of the devices (ESI S6†) in combination with the improved device hole charge carrier mobility and the DC conductivity as shown earlier. Thus, it is more evidence that the UV-Ozone treatment has a beneficial effect on the device performance of OSCs, making MoO_x a candidate for HTL in efficient OSCs.

Light soaking stability measurements

We also investigated the stability of the optimized PM6:Y6 OSCs based on the highest PCE HTLs by performing light-soaking measurements, which is important in the commercialization of NFA-based OSCs. The devices were characterized under nitrogen conditions while being exposed to continuous white colour (6500 K) light-emitting diode (LED) source with light intensity equivalent to ~1 sun (100 mW cm^{-2}) at 55 °C. The normalized figures of merit (*i.e.* normalized PCE, FF, J_{sc} and V_{oc}) of the cells plotted as a function of light-soaking time are presented in Fig. 9. After 100 hours of continuous light soaking, the UV-Ozone-treated and the pristine MoO_x-based device retained ~65% and 58% of their

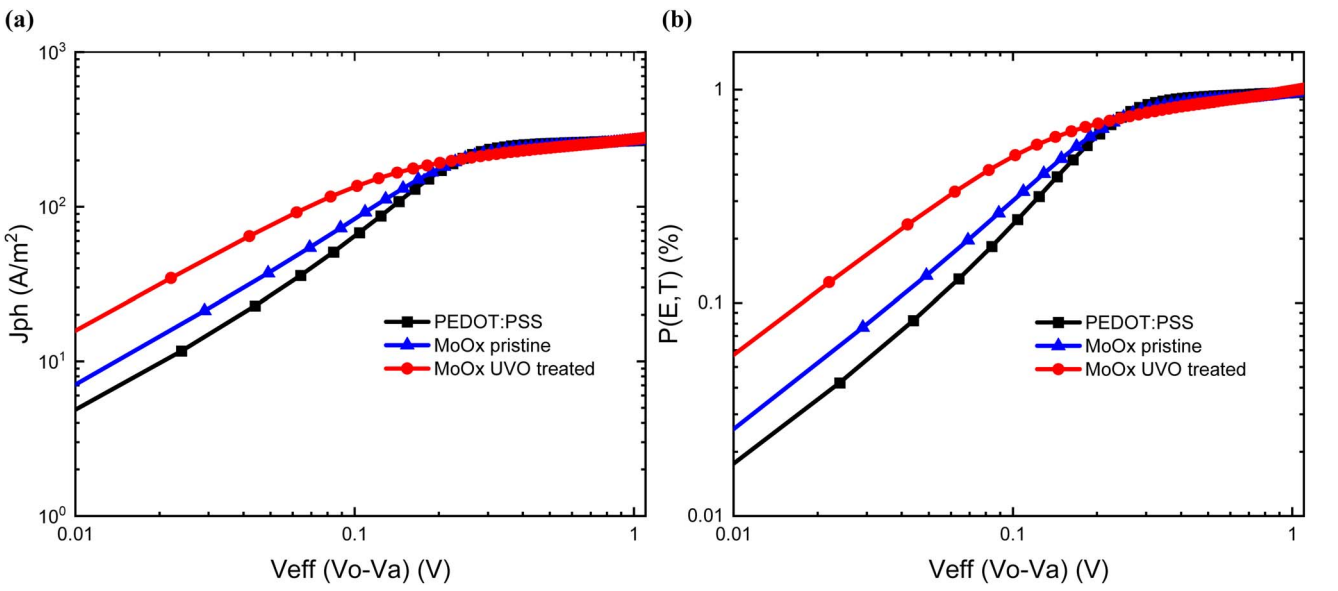

Fig. 8 (a) Photocurrent density (J_{ph}) *versus* effective voltage (V_{eff}) curves of PM6:Y6 devices incorporating different HTLs. (b) Charge collection probabilities $P(E, T)$ curves of PM6:Y6 devices incorporating different HTLs.

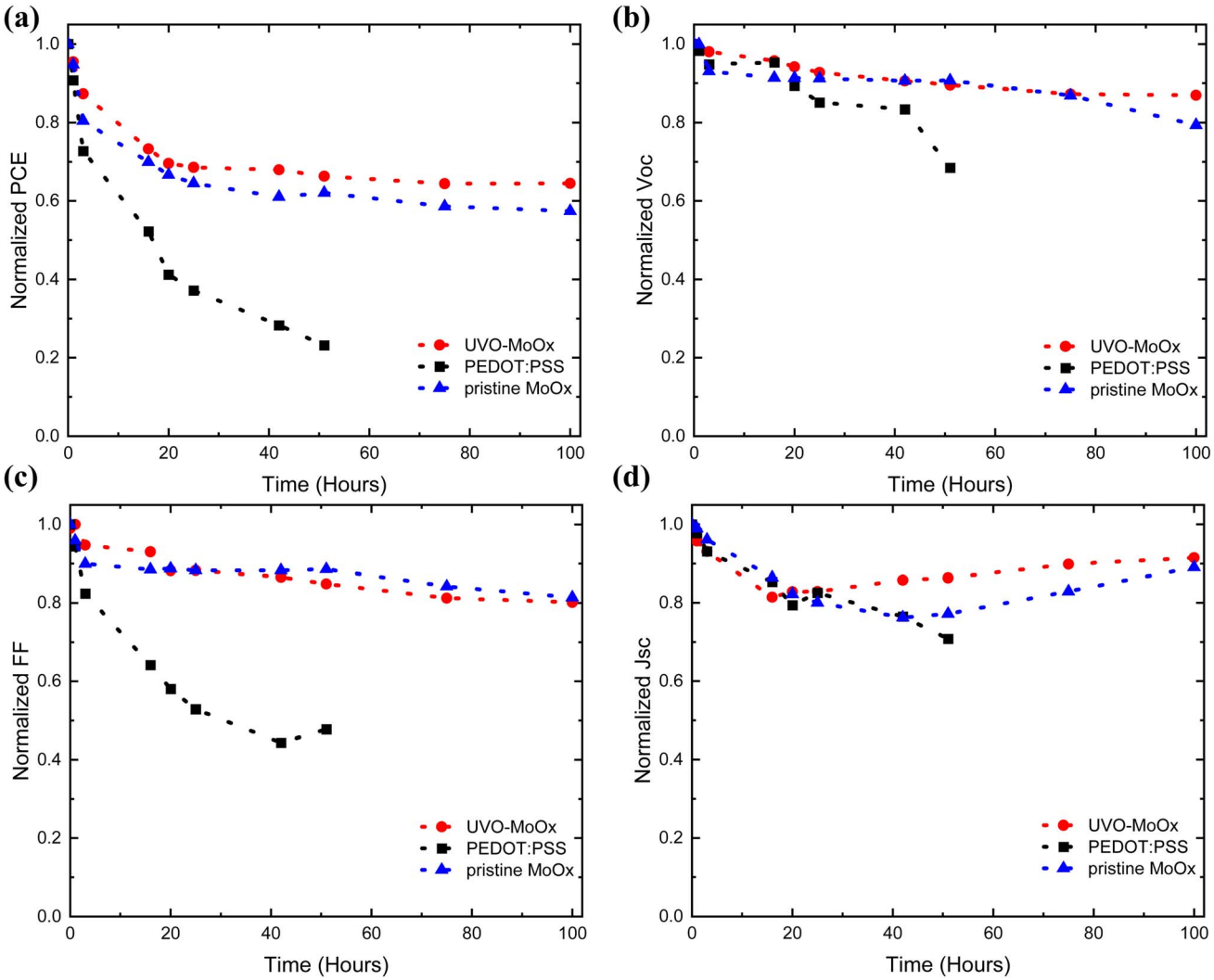

Fig. 9 Normalized (a) PCE, (b) V_{oc}, (c) FF and (d) J_{sc} over time graphs of light soaking test of PM6:Y6 solar cells based on UVO-treated MoO_x and pristine MoO_x *versus* PEDOT:PSS.

initial PCE respectively, while the performance of the PEDOT:PSS-based counterpart deteriorated rapidly to 23% of its initial PCE after only 51 hours. Thus, both MoO_x HTLs are fundamentally more stable than the PEDOT:PSS counterpart, while the efficiency improvement of treated cells compared to pristine originates from the UV-Ozone treatment process. This striking difference in the Fig. 9(c) (dependence of FF with time), explains well the significance of our work towards stable OSCs. In particular, stabilised FF over time of both MoO_x-based cells imply stable and intact interface.[72] In our results we observe that the control samples' (PEDOT:PSS) FF decrease very fast and is the main reason for the fast drop of the PCE. On the contrary, our target devices (UV-Ozone-treated and pristine MoO_x devices) present a much firmer FF trend over time and is the key reason for the more stable PCE with time. Although preliminary, the results indicate that ITO/UVO-treated MoO_x could significantly enhance the lifetime stability and operation of state-of-the-art OSCs (the key issue of OSCs towards the commercialisation) as shown in ESI Fig. S7(a)–(c)† from the representative time depended *J–V* curves.

Light depended measurements

Next, we performed *J–V* light-intensity-dependence measurements to understand the impact of light-soaking on PEDOT:PSS-based and UV-Ozone-treated MoO_x-based OSCs since both architectures present the highest PCE values in this case study. Measuring and tracking the V_{oc} *versus* the light intensity can be used to extract the light ideality factor (n). The n is a measure of whether the recombination type is Shockley–Read–Hall (SRH ($n = 2$) or bimolecular ($n = 1$).[70] The n values in each case were calculated based on the Shockley equation (under the assumption that the photocurrent scales linearly with the light intensity and photocurrent/saturation current $\gg$ 1:

$$V_{oc} = n\frac{q}{kT}\frac{dV_{oc}}{d(\ln(L))}$$

where, n is the light ideality factor, k is the Boltzmann constant, T is the temperature, and q is the unit charge.

The dependence of V_{oc} *versus* the light intensity before the light soaking test (ESI S10(a) and S11(a)†) for PEDOT:PSS-based

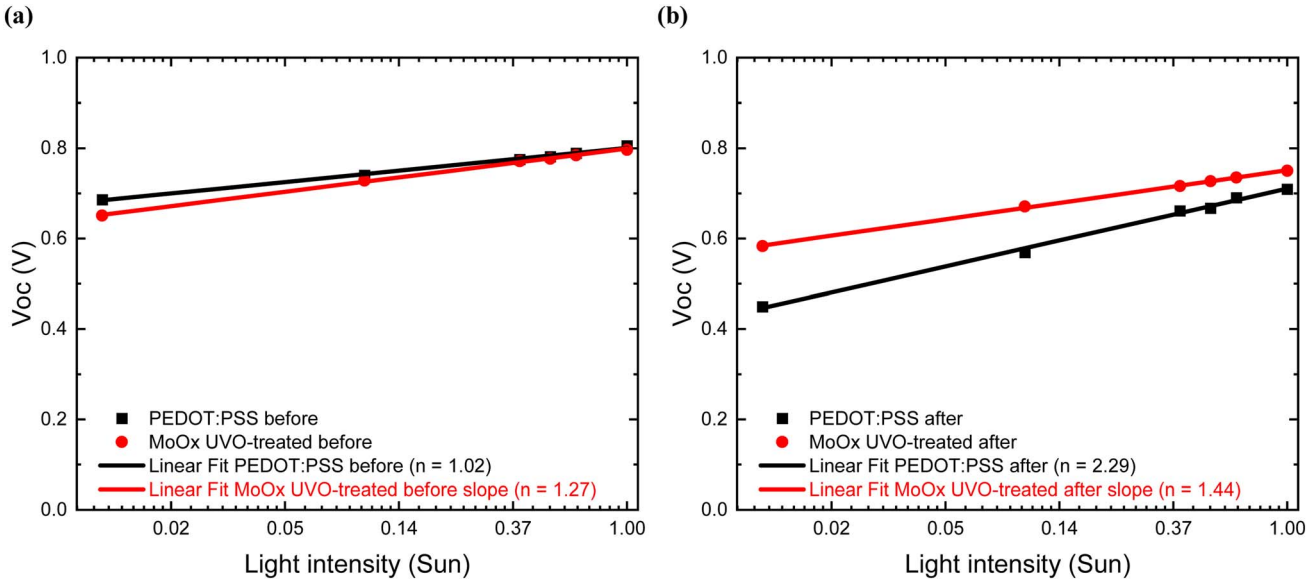

Fig. 10 (a) V_{OC} *versus* light dependence measurements of PM6:Y6 solar cells based on incorporating the different HTLs, before light soaking test, (b) V_{OC} *versus* light dependence measurements of PM6:Y6 solar cells based on incorporating the different HTLs after light soaking test.

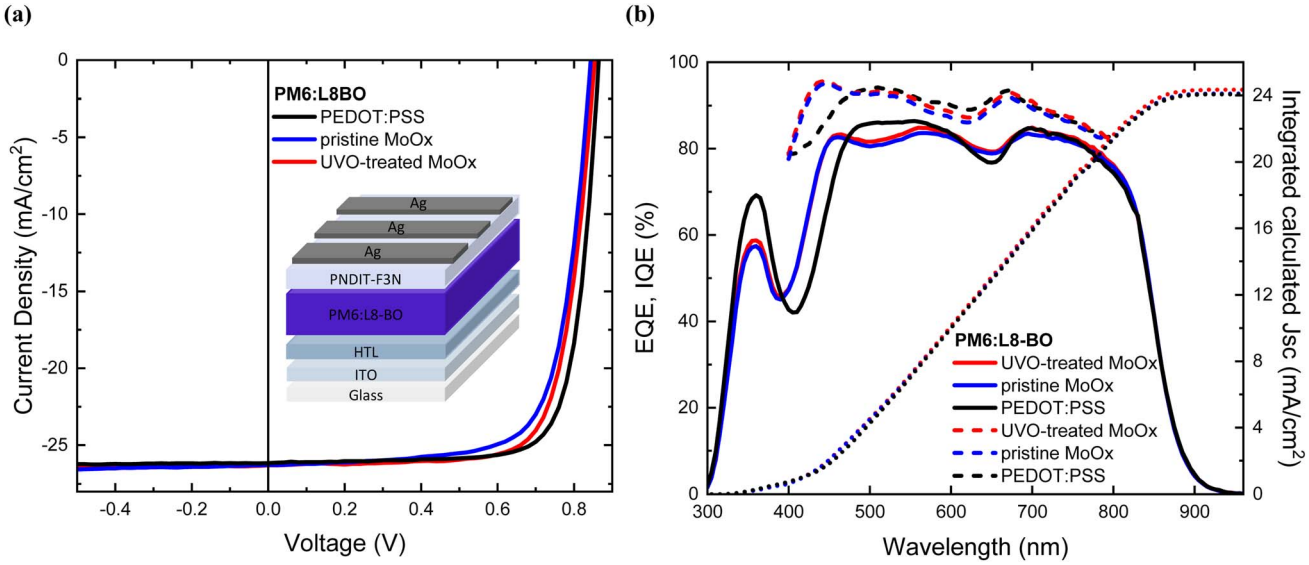

Fig. 11 (a) *J*–*V* curves of champion cells PM6:L8BO solar cells incorporating different HTLs, (b) EQE and IQE spectra of PM6:L8BO solar cells incorporating different HTLs.

and UV-Ozone-treated MoO_x-based devices presented slope values of n 1.02 and 1.27, respectively, as shown in Fig. 10(a). The lower n value of devices with PEDOT:PSS compared to the UVO-treated MoO_x matches with the higher initial PCE of the devices before the stability test. Interestingly, a higher slope value, which leads to an inferior ideality factor, was observed after 51 hours in the case of PEDOT:PSS-based devices with an increase of 124% and n value of 2.29 (practically the PEDOT:PSS-based devices are fully degraded after 51 hours of exposure in the stability test) (see ESI S10(b)†). On the other hand, the UV-Ozone-treated MoO_x-based cells (ESI S11(b)†), demonstrated a significantly lower increase of just 13% and an n value of 1.44, implying that these devices are fully functional and only slightly degraded. This suggests that more severe trap-assisted recombination occurs on PEDOT:PSS-based cells as the devices degrade,[73,74] in contrast to the UV-Ozone-treated MoO_x-based cells, demonstrating their better stability under light-soaking conditions. The significant increase of the ideality factor in PEDOT:PSS-based devices can further be supported by the rapid decrease of the FF factor over time since the FF can be described as the interplay between recombination and charge extraction processes in solar cells.[75,76] More specifically, for the PEDOT:PSS cells, after 51 hours of light soaking, the FF reached values less than 50% of its initial value, while the UV-Ozone-

Table 5 Photovoltaic parameters of PM6:L8BO PEDOT:PSS, pristine-MoO_x, and UV-Ozone-treated MoO_x-based, mean values and champion device performance in brackets

HTL	V_{oc} mean ($V_{oc\ hero}$) (V)	J_{sc} mean ($J_{sc\ hero}$) (mA cm^{-2})	J_{sc} EQE (mA cm^{-2})	FF mean (FF_{hero})	PCE mean (PCE_{hero}) (%)
PEDOT:PSS	0.86 (0.86)	25.54 (26.17)	24.10	76.82 (77.10)	17.0 (17.35)
Pristine-MoO_x	0.85 (0.85)	25.90 (26.28)	24.12	72.37 (72.60)	15.93 (16.21)
UVO-treated MoO_x	0.85 (0.86)	26.05 (26.31)	24.32	74.28 (74.90)	16.47 (16.85)

treated MoO_x cells retained almost 85% of its initial value. Considering that the main function of photovoltaic cells is to provide power to a load, it highlighted that the UV-Ozone-treated device exhibited longer stable power output values after 100 hours of light soaking (see ESI S8(a) and (b)†).

Broader applicability

Finally, we investigate the broader applicability of the UV-Ozone treatment on thermally evaporated MoO_x HTL in another highly efficient BHJ system. For this purpose, we selected PM6:L8BO with PCE values beyond 17%, as reported in the literature.[2,77] The results of the UV-Ozone treatment on MoO_x demonstrated an equal impact on the PM6:L8BO devices, as observed in the case of the PM6:Y6 BHJ system. Representative *J–V* curves obtained from the champion cells using different HTLs are shown in Fig. 11(a), a summary of the champion data and mean device photovoltaic parameters is provided in Table 5. The statistical analysis of the devices from 5 individual cells (see ESI S9†).

The PEDOT:PSS-based PM6:L8BO demonstrated a PCE of 17.35% with a V_{oc} of 0.86 V, J_{sc} 26.17 mA cm^{-2} and an FF of 77.10 in line with the literature. On the other hand, pristine MoO_x cells exhibited a maximum efficiency of 16.21% with J_{sc} of 26.28 mA cm^{-2}, V_{oc} of 0.85 V, and FF of 72.60. Notably, the UV-Ozone-treatment enhanced the performance of the pristine MoO_x, demonstrating a maximum PCE of 16.85%, accompanied by a J_{sc} of 26.31 mA cm^{-2}, an improved FF of 74.90 and V_{oc} of 0.85 V. As a result, a noteworthy PCE increase of 3.95% compared to the pristine MoO_x-based OSCs and the highest reported value to the best our knowledge for MoO_x-based binary OSCs in the literature with an active area of ~0.1 cm^2.

From the EQE spectra as shown in Fig. 11(b), the calculated photocurrent densities follow similar trend (within ±7% for all devices difference) to those measured from the *J–V* curves with a solar simulator. The photocurrent values extracted from EQE spectra are consistent with the results based on the transmission spectra Fig. 1(b) demonstrated earlier. Similarly, the IQE measurements indicate that the UV-Ozone-treated MoO_x-based devices exhibit a more efficient internal photon-to-electron conversion compared to the pristine MoO_x-based OSCs. The average IQE value for these treated cells is 90%, with peak values reaching 96% and 93% at wavelengths of 450 nm and 665 nm, respectively. In contrast, the pristine MoO_x-based cells show an average IQE value of 88%, with maximum values of 95% and 91% at the same wavelengths. The above results are in full agreement with findings mentioned earlier (IQE of PM6:Y6-based cells) that a larger number of absorbed photons is successfully converted into electrons, that contribute to current generation in the case of the UV-Ozone-treated MoO_x-based cells in contrast with the pristine-based devices.

Conclusions

This study presents a comprehensive strategy aimed at enhancing the electrical and physical characteristics of MoO_x-based HTL utilized in OSCs. The strategy involves a post-UV-Ozone treatment of the MoO_x HTL, rendering it particularly beneficial for applications beyond photovoltaic technologies. Initially, we optimized both the thickness of the MoO_x layer and the exposure time of the UV-Ozone treatment. Our findings suggest that an optimal MoO_x thickness of 5 nm requires only 2.5 minutes of UV-Ozone exposure to achieve a notable enhancement in the electrical properties of the film. This treatment resulted in a 0.2 eV increase (in absolute values) in the work function of MoO_x, attributed to alterations in the oxidation states of the material. Consequently, we observed an increase in hole mobilities, more balanced mobility ratios and an improvement in DC conductivity compared to pristine MoO_x films. Additionally, the hydrophilicity of the MoO_x film surface was markedly enhanced post-treatment, leading to better wetting of the subsequently applied photoactive layer. EIS in conjunction with IQE, charge collection probabilities and the PL characterisation revealed an improved interface between the UV-Ozone-treated MoO_x and the photoactive layer, as indicated by longer charge carrier lifetimes, improved charge collection with a substantial 15% PL quenching, respectively. Furthermore, devices incorporating pristine and UV-Ozone-treated MoO_x based OSCs exhibited significantly improved operational stability, maintaining approximately 58% and 65% of their initial performance after 100 hours, respectively. In contrast, devices based on PEDOT:PSS experienced rapid degradation, dropping to 23% of their pre-aging performance after 51 hours of light exposure at 55 °C, ultimately leading to complete failure. The enhanced stability of the high efficiency UV-Ozone-treated MoO_x-based devices is attributed to minimal changes in the ideality factor and their ability to sustain high fill factor values (85% of initial values) after 100 hours. This approach serves as a catalyst for simultaneous high performance and stability relative to the control PEDOT:PSS-based cells, which demonstrate high efficiency but markedly shorter lifetime stability. Ultimately, the study highlighted the broad applicability of the UV-Ozone-treated MoO_x HTL in OSCs that employ the highly efficient PM6:L8BO BHJ system. This system achieved a PCE of 16.85%, representing the highest efficiency recorded to date for binary OSCs utilizing metal oxide-based

HTLs. Our findings underscore the potential for tuning the physicochemical characteristics of metal transition oxides to drive future innovations in device architecture and advanced surface engineering strategies.

Data availability

The data supporting this article have been included as part of the ESI.†

Author contributions

A. P. and G. K. conceived the idea. A. P., G. K. and S. R. P. S discussed, planned the content, analysed the literature. A. P. designed, fabricated and characterized the devices. A. L. assisted with the Kelvin Probe measurements. K. A. performed the EIS measurements and analyzed the data. A. P., G. K. contributed to the relevant data analysis and the revision of the first draft. A. P., G. K., K. A., D. K. and S. R. P. S., contributed to the preparation of the manuscript. S. R. P. S. supervised the project. All authors contributed to manuscript preparation, revision and approved its submission for publication.

Conflicts of interest

There are no conflicts to declare.

Acknowledgements

A. P. acknowledge the funding from UKRI (iCase/UKRI) studentship grant number is EP/T517616. A. P. and S. R. P. S. gratefully acknowledge the support of QinetiQ and MUSICODE H2020, the European collaborative research and innovation project led by multi-disciplinary consortium. G. K. gratefully acknowledge the support from the Hellenic Mediterranean University and the Department of Electronics Engineering.

References

1 NREL, Best Research Cell Efficiency Chart, https://www.nrel.gov/pv/assets/pdfs/best-research-cell-efficiencies.
2 L. Zhu, M. Zhang, J. Xu, C. Li, J. Yan, G. Zhou, W. Zhong, T. Hao, J. Song, X. Xue, Z. Zhou, R. Zeng, H. Zhu, C. C. Chen, R. C. I. MacKenzie, Y. Zou, J. Nelson, Y. Zhang, Y. Sun and F. Liu, *Nat. Mater.*, 2022, **21**, 656–663.
3 R. Sun, Y. Wu, X. Yang, Y. Gao, Z. Chen, K. Li, J. Qiao, T. Wang, J. Guo, C. Liu, X. Hao, H. Zhu and J. Min, *Adv. Mater.*, 2022, **34**, 2110147.
4 A. Panagiotopoulos, T. Maksudov, G. Kakavelakis, G. Perrakis, E. A. Alharbi, D. Kutsarov, F. H. Isikgor, S. Alfihed, K. Petridis, M. Kafesaki, S. R. P. Silva, T. D. Anthopoulos and M. Graetzel, *Appl. Phys. Rev.*, 2023, **10**, 41303.
5 A. Seitkhan, M. Neophytou, M. Kirkus, E. Abou-Hamad, M. N. Hedhili, E. Yengel, Y. Firdaus, H. Faber, Y. Lin, L. Tsetseris, I. McCulloch and T. D. Anthopoulos, *Adv. Funct. Mater.*, 2019, **29**, 1905810.
6 W. Y. Tan, R. Wang, M. Li, G. Liu, P. Chen, X. C. Li, S. M. Lu, H. L. Zhu, Q. M. Peng, X. H. Zhu, W. Chen, W. C. H. Choy, F. Li, J. Peng and Y. Cao, *Adv. Funct. Mater.*, 2014, **24**, 6540–6547.
7 Z.-G. Zhang, B. Qi, Z. Jin, D. Chi, Z. Qi, Y. Li and J. Wang, *Energy Environ. Sci.*, 1966–1973, 2014, DOI: 10.1039/c4ee00022f.
8 F. Huang, H. Wu, D. Wang, W. Yang and Y. Cao, *Chem. Mater.*, 2004, **16**, 708–716.
9 C. E. Small, S. Chen, J. Subbiah, C. M. Amb, S. W. Tsang, T. H. Lai, J. R. Reynolds and F. So, *Nat. Photonics*, 2011, **6**, 115–120.
10 K. D. G. I. Jayawardena, R. Rhodes, K. K. Gandhi, M. R. R. Prabhath, G. D. M. R. Dabera, M. J. Beliatis, L. J. Rozanski, S. J. Henley and S. R. P. Silva, *J. Mater. Chem. A*, 2013, **1**, 9922–9927.
11 Y. Lin, Y. Firdaus, M. I. Nugraha, F. Liu, S. Karuthedath, A. H. Emwas, W. Zhang, A. Seitkhan, M. Neophytou, H. Faber, E. Yengel, I. McCulloch, L. Tsetseris, F. Laquai and T. D. Anthopoulos, *Adv. Sci.*, 2020, 1903419, DOI: 10.1002/ADVS.201903419.
12 G. Cai, Z. Chen, X. Xia, Y. Li, J. Wang, H. Liu, P. P. Sun, C. Li, R. Ma, Y. Zhou, W. Chi, J. Zhang, H. Zhu, J. Xu, H. Yan, X. Zhan and X. Lu, *Adv. Sci.*, 2022, 2200578, DOI: 10.1002/ADVS.202200578.
13 R. A. Hatton, N. P. Blanchard, L. W. Tan, G. Latini, F. Cacialli and S. R. P. Silva, *Org. Electron.*, 2009, **10**, 388–395.
14 C. T. G. Smith, R. W. Rhodes, M. J. Beliatis, K. D. G. Imalka Jayawardena, L. J. Rozanski, C. A. Mills and S. R. P. Silva, *Appl. Phys. Lett.*, 2014, **105**, 73304.
15 G. D. M. R. Dabera, K. D. G. I. Jayawardena, M. R. R. Prabhath, I. Yahya, Y. Y. Tan, N. A. Nismy, H. Shiozawa, M. Sauer, G. Ruiz-Soria, P. Ayala, V. Stolojan, A. A. D. T. Adikaari, P. D. Jarowski, T. Pichler and S. R. P. Silva, *ACS Nano*, 2013, **7**, 556–565.
16 Z. Zheng, Q. Hu, S. Zhang, D. Zhang, J. Wang, S. Xie, R. Wang, Y. Qin, W. Li, L. Hong, N. Liang, F. Liu, Y. Zhang, Z. Wei, Z. Tang, T. P. Russell, J. Hou and H. Zhou, *Adv. Mater.*, 2018, 1801801, DOI: 10.1002/ADMA.201801801.
17 M. Zeng, X. Wang, R. Ma, W. Zhu, Y. Li, Z. Chen, J. Zhou, W. Li, T. Liu, Z. He, H. Yan, F. Huang and Y. Cao, *Adv. Energy Mater.*, 2020, **10**, 2000743.
18 Y. Wang, J. Han, L. Cai, N. Li, Z. Li and F. Zhu, *J. Mater. Chem. A*, 2020, **8**, 21255–21264, DOI: 10.1039/d0ta08018g.
19 M. P. De Jong, L. J. Van Ijzendoorn and M. J. A. De Voigt, *Appl. Phys. Lett.*, 2000, **77**, 2255–2257.
20 N. Wijeyasinghe, A. Regoutz, F. Eisner, T. Du, L. Tsetseris, Y. H. Lin, H. Faber, P. Pattanasattayavong, J. Li, F. Yan, M. A. McLachlan, D. J. Payne, M. Heeney and T. D. Anthopoulos, *Adv. Funct. Mater.*, 2017, **27**, 1701818.
21 Z. Li, H. Huang, X. Zeng, B. Deng, C. Li, C. Gao, G. Zhang, S. Li and C. Xie, *Org. Electron.*, 2024, **133**, 107104.
22 C. Girotto, E. Voroshazi, D. Cheyns, P. Heremans and B. P. Rand, *ACS Appl. Mater. Interfaces*, 2011, **3**, 3244–3247.
23 W. Feng, C. Song, X. Hu, S. Liu, R. Yi, X. Yang, H. Yan and X. Hou, *ACS Appl. Mater. Interfaces*, 2018, **10**, 9.

24 J. Meyer, S. Hamwi, M. Kröger, W. Kowalsky, T. Riedl and A. Kahn, *Adv. Mater.*, 2012, **24**, 5408–5427.
25 D. I. Kutsarov, E. New, F. Bausi, A. Zoladek-Lemanczyk, F. A. Castro and S. R. P. Silva, *Sol. Energy Mater. Sol. Cells*, 2017, **161**, 388–396.
26 K. E. Lee, L. Liu and T. L. Kelly, *J. Phys. Chem. C*, 27735–27741, 2014, DOI: 10.1021/jp508972v.
27 M. D. Irwin, D. B. Buchholz, A. W. Hains, R. P. H. Chang and T. J. Marks, *Proc. Natl. Acad. Sci. U. S. A.*, 2008, **105**, 2783–2787.
28 R. Remya, P. T. G. Gayathri and B. Deb, *Mater. Chem. Phys.*, 2020, **255**, 123584.
29 R. Miclette Lamarche, A. Gasonoo, A. Hoff, R. Chernikov, G. C. Welch and S. Trudel, *Chem. Mater.*, 2023, **35**, 2353–2362.
30 Y. Li, P. Li, M. Qu, F. Liu, B. Wei and G. Chen, *Nanotechnology*, 2023, **34**, 285205, DOI: 10.1088/1361-6528/acccfc.
31 C. Seiichiro Murase, Y. Yang, S. Murase and Y. Yang, *Adv. Mater.*, 2012, **24**, 2459–2462.
32 F. Cheng, G. Fang, X. Fan, H. Huang, Q. Zheng, P. Qin, H. Lei and Y. Li, *Sol. Energy Mater. Sol. Cells*, 2013, **110**, 63–68.
33 K. O. Brinkmann, T. Becker, F. Zimmermann, C. Kreusel, T. Gahlmann, M. Theisen, T. Haeger, S. Olthof, C. Tückmantel, M. Günster, T. Maschwitz, F. Göbelsmann, C. Koch, D. Hertel, P. Caprioglio, F. Peña-Camargo, L. Perdigón-Toro, A. Al-Ashouri, L. Merten, A. Hinderhofer, L. Gomell, S. Zhang, F. Schreiber, S. Albrecht, K. Meerholz, D. Neher, M. Stolterfoht and T. Riedl, *Nature*, 2022, 280, DOI: 10.1038/s41586-022-04455-0.
34 W. Hadmojo, F. Isikgor, Y. Lin, Z. Ling, Q. He, H. Faber, E. Yengel, R. Ali, A. Samad, R. Enggar Anugrah Ardhi, S. Jeong, H. Young Woo, U. Schwingenschlögl, M. Heeney, T. Anthopoulos, W. Tantyo Hadmojo, F. H. Isikgor, S. Young Jeong, T. D. Anthopoulos and C. Authors, *Energy Environ. Mater.*, 2024, **7**, e12712.
35 Y. Wang, Z. Shi, H. Liu, F. Wang, Y. Bai, X. Bian, B. Zhang, T. Hayat, A. Alsaedi and Z. Tan, *Polymers*, 2017, **9**, 571.
36 X. Hou, Q. Li, T. Cheng, L. Yu, F. Wang, J. Lin, S. Dai, Y. Li and Z. Tan., *J. Mater. Chem. A*, 2015, **3**, 18727–18734, DOI: 10.1039/c5ta03967c.
37 W. J. Dong, G. H. Jung and J. L. Lee, *Sol. Energy Mater. Sol. Cells*, 2013, **116**, 94–101.
38 W. Huang, H. Fan, X. Zhuang and J. Yu, *Nanoscale Res. Lett.*, 2014, **9**, 1–8.
39 J. R. Vig, *J. Vac. Sci. Technol., A*, 1985, **3**, 1027–1034.
40 K. Sugiyama, H. Ishii, Y. Ouchi and K. Seki, *J. Appl. Phys.*, 2000, **87**, 295–298.
41 A. W. Hains, J. Liu, A. B. F. Martinson, M. D. Irwin and T. J. Marks, *Adv. Funct. Mater.*, 2010, **20**, 595–606.
42 *Hardware: Series 10 Software: Series 11 KP manual 2021 Non-scanning Kelvin probe system manual: For software series 11 and hardware version KP020 (Win 10)*.
43 C. Melios, A. Centeno, A. Zurutuza, V. Panchal, C. E. Giusca, S. Spencer, S. R. P. Silva and O. Kazakova, *Carbon*, 2016, **103**, 273–280.
44 P. C. Kao, C. J. Hsieh, Z. H. Chen and S. H. Chen, *Sol. Energy Mater. Sol. Cells*, 2018, **186**, 131–141.
45 C. Lattyak, K. Gehrke and M. Vehse, *J. Phys. Chem. C*, 2022, **126**, 13929–13935.
46 X. Wu, D. Zhang, B. Liu, Y. Wang, X. Wang, Q. Liu, D. Gao, N. Wang, B. Li, L. Wang, Z. Yu, X. Li, S. Xiao, N. Li, M. Stolterfoht, Y. H. Lin, S. Yang, X. C. Zeng and Z. Zhu, *Adv. Mater.*, 2024, 2410692.
47 H. Bin, K. Datta, J. Wang, T. P. A. Van Der Pol, J. Li, M. M. Wienk and R. A. J. Janssen, *ACS Appl. Mater. Interfaces*, 2022, **14**, 16497–16504.
48 J. Wu, H. Cha, T. Du, Y. Dong, W. Xu, C. T. Lin and J. R. Durrant, *Adv. Mater.*, 2022, 2101833, DOI: 10.1002/ADMA.202101833.
49 J. Yuan, Y. Zhang, L. Zhou, G. Zhang, H.-L. Yip, T.-K. Lau, X. Lu, C. Zhu, H. Peng, P. A. Johnson, M. Leclerc, Y. Cao, J. Ulanski, Y. Li and Y. Zou, *Joule*, 2019, **3**, 1140–1151.
50 A. Domínguez, C. Ramos, A. Dutt, G. Santana, Y. Kudriavtsev and O. de Melo, *Mater. Lett.*, 2022, **318**, 132171.
51 B. Paci, G. Kakavelakis, A. Generosi, J. Wright, C. Ferrero, E. Stratakis and E. Kymakis, *Sol. Energy Mater. Sol. Cell.*, 2017, **159**, 617–624, DOI: 10.1016/j.solmat.2016.01.003.
52 B. Paci, G. Kakavelakis, A. Generosi, V. Rossi Albertini, J. P. Wright, C. Ferrero, D. Konios, E. Stratakis and E. Kymakis, *RSC Adv.*, 2015, **5**, 106930–106940.
53 G. Kakavelakis, A. E. D. R. Castillo, V. Pellegrini, A. Ansaldo, P. Tzourmpakis, R. Brescia, M. Prato, E. Stratakis, E. Kymakis and F. Bonaccorso, *ACS Nano*, 2017, **11**(4), 3517–3531, DOI: 10.1021/acsnano.7b00323.
54 R. Yu, H. Yao, Y. Cui, L. Hong, C. He, J. Hou, R. Yu, H. Yao, Y. Cui, L. Hong, C. He and J. Hou, *Adv. Mater.*, 2019, **31**, 1902302.
55 C. Xie, X. Zeng, C. Li, X. Sun, S. Liang, H. Huang, B. Deng, X. Wen, G. Zhang, P. You, C. Yang, Y. Han, S. Li, G. Lu, H. Hu, N. Li and Y. Chen, *Energy Environ. Sci.*, 2024, **17**, 2441–2452.
56 C. M. Proctor, J. A. Love, T.-Q. Nguyen, C. M. Proctor, J. A. Love and T.-Q. Nguyen, *Adv. Mater.*, 2014, **26**, 5957–5961.
57 P. Robaeys, F. Bonaccorso, E. Bourgeois, J. D'Haen, W. Dierckx, W. Dexters, D. Spoltore, J. Drijkoningen, J. Liesenborgs, A. Lombardo, A. C. Ferrari, F. Van Reeth, K. Haenen, J. V. Manca and M. Nesladek, *Appl. Phys. Lett.*, 2014, **105**, 83306.
58 C. Xie, X. Zeng, C. Li, X. Sun, S. Liang, H. Huang, B. Deng, X. Wen, G. Zhang, P. You, C. Yang, Y. Han, S. Li, G. Lu, H. Hu, N. Li and Y. Chen, *Energy Environ. Sci.*, 2024, **17**, 2441–2452.
59 G. Garcia-Belmonte, A. Munar, E. M. Barea, J. Bisquert, I. Ugarte and R. Pacios, *Org. Electron.*, 2008, **9**, 847–851.
60 E. Von Hauff, *J. Phys. Chem. C*, 2019, **123**, 11329–11346.
61 E.-P. Yao, C.-C. Chen, J. Gao, Y. Liu, Q. Chen, M. Cai, W.-C. Hsu, Z. Hong, G. Li and Y. Yang, *Sol. Energy Mater. Sol. Cell.*, 2014, **130**, 20–26, DOI: 10.1016/j.solmat.2014.05.049.
62 Y. Lin, A. Magomedov, Y. Firdaus, D. Kaltsas, A. El-Labban, H. Faber, D. R. Naphade, E. Yengel, X. Zheng, E. Yarali, N. Chaturvedi, K. Loganathan, D. Gkeka,

S. H. AlShammari, O. M. Bakr, F. Laquai, L. Tsetseris, V. Getautis and T. D. Anthopoulos, *ChemSusChem*, 2021, **14**, 3569–3578.

63 S. Braun, W. R. Salaneck and M. Fahlman, *Adv. Mater.*, 2009, **21**, 1450–1472.

64 C. Xie, T. Heumüller, W. Gruber, X. Tang, A. Classen, I. Schuldes, M. Bidwell, A. Späth, R. H. Fink, T. Unruh, I. McCulloch, N. Li and C. J. Brabec, *Nat. Commun.*, 2018, **9**, 1–11.

65 C. Wöpke, C. Göhler, M. Saladina, X. Du, L. Nian, C. Greve, C. Zhu, K. M. Yallum, Y. J. Hofstetter, D. Becker-Koch, N. Li, T. Heumüller, I. Milekhin, D. R. T. Zahn, C. J. Brabec, N. Banerji, Y. Vaynzof, E. M. Herzig, R. C. I. MacKenzie and C. Deibel, *Nat. Commun.*, 2022, **13**, 1–8.

66 A. C. Hurd, A. Alotaibi, A. Patterson, O. Alqahtani, J. Doyle, B. Akira, A. C. Authors Ally Hurd and B. Akira Collins, *Macalester Journal of Physics and Astronomy*, 2020, 9.

67 C. M. Proctor, M. Kuik and T. Q. Nguyen, *Prog. Polym. Sci.*, 2013, **38**, 1941–1960.

68 G. Kakavelakis, I. Vangelidis, A. Heuer-Jungemann, A. G. Kanaras, E. Lidorikis, E. Stratakis and E. Kymakis, *Adv. Energy Mater.*, 2016, 1501640, DOI: **10.1002/AENM.201501640**.

69 C. G. Shuttle, R. Hamilton, B. C. O'Regan, J. Nelson and J. R. Durrant, *Proc. Natl. Acad. Sci. U. S. A.*, 2010, **107**, 16448–16452.

70 V. D. Mihailetchi, L. J. A. Koster, J. C. Hummelen and P. W. M. Blom, *Phys. Rev. Lett.*, 2004, **93**, 216601, DOI: **10.1103/PhysRevLett.93.216601**.

71 J.-L. Wu, F.-C. Chen, Y.-S. Hsiao, F.-C. Chien, P. Chen, C.-H. Kuo, M. H. Huang and C.-S. Hsu, *ACS Nano*, 2011, **5**, 959–967, DOI: **10.1021/nn102295p**.

72 L. Ciammaruchi, R. Oliveira, A. Charas, Tulus, E. Von Hauff, G. Polino, F. Brunetti, R. Hansson, E. Moons, M. Krassas, G. Kakavelakis, E. Kymakis, J. G. Sánchez, J. Ferre-Borrull, L. F. Marsal, S. Züfle, D. Fluhr, R. Roesch, T. Faber, U. S. Schubert, H. Hoppe, K. Bakker, S. Veenstra, G. Zanotti, E. A. Katz, P. Apilo, B. Romero, T. A. Tumay, E. Parlak, L. M. Stagno, V. Turkovic, H. G. Rubahn, M. Madsen, V. Kažukauskas, D. M. Tanenbaum, S. Shanmugam and Y. Galagan, *J. Mater. Res.*, 2018, **33**, 1909–1924.

73 C. M. Proctor and T.-Q. Nguyen, *Appl. Phys. Lett.*, 2015, **106**, 83301.

74 D. Neher, J. Kniepert, A. Elimelech and L. J. A. Koster, *Sci. Rep.*, 2016, **6**, 1–9.

75 C. Wöpke, C. Göhler, M. Saladina, X. Du, L. Nian, C. Greve, C. Zhu, K. M. Yallum, Y. J. Hofstetter, D. Becker-Koch, N. Li, T. Heumüller, I. Milekhin, D. R. T. Zahn, C. J. Brabec, N. Banerji, Y. Vaynzof, E. M. Herzig, R. C. I. MacKenzie and C. Deibel, *Nat. Commun.*, 2022, **13**, 4475.

76 D. Bartesaghi, I. D. C. Pérez, J. Kniepert, S. Roland, M. Turbiez, D. Neher and L. J. A. Koster, *Nat. Commun.*, 2015, **6**, 1–10.

77 X. Zeng, T. Xu, H. Chen, B. Deng, Q. Yan, X. Wen, Z. Li, H. Zeng, C. Gao, Y. Xiao, J. Liao, H. Liu, B. He, P. Han, G. Zhang, S. Li, Y. Chen and C. Xie, *Energy Environ. Sci.*, 2024, **17**, 9383–9393.